*Article*

# Structure and Interdigitation of Chain-Asymmetric Phosphatidylcholines and Milk Sphingomyelin in the Fluid Phase

**Moritz PK Frewein [1,2,3,4], Milka Doktorova [5], Frederick A Heberle [6], Haden L Scott [7,8], Enrico F Semeraro [1,3,4], Lionel Porcar [2] and Georg Pabst [1,3,4]***

1 University of Graz, Institute of Molecular Biosciences, NAWI Graz, 8010 Graz, Austria
2 Institut Laue-Langevin, 38043 Grenoble, France
3 BioTechMed Graz, 8010 Graz, Austria
4 Field of Excellence BioHealth – University of Graz, 8010 Graz, Austria
5 Department of Molecular Physiology and Biological Physics, University of Virginia School of Medicine, Charlottesville, VA 22903, USA
6 Department of Chemistry, University of Tennessee Knoxville, Knoxville, TN 37996, USA
7 Center for Environmental Biotechnology, University of Tennessee, Knoxville, TN 37996, USA
8 Shull Wollan Center, Oak Ridge National Laboratory, Oak Ridge, TN 37831, USA
* Correspondence: georg.pabst@uni-graz.at; Tel.: +43 316 380 4989

**Abstract:** We addressed the frequent occurrence of mixed-chain lipids in biological membranes and their impact on membrane structure by studying several chain-asymmetric phosphatidylcholines and the highly asymmetric milk sphingomyelin. Specifically, we report trans-membrane structures of the corresponding fluid lamellar phases using small-angle X-ray and neutron scattering, which were jointly analyzed in terms of a membrane composition-specific model, including a headgroup hydration shell. Focusing on terminal methyl groups at the bilayer center we found a linear relation between hydrocarbon chain length mismatch and the methyl-overlap for phosphatidylcholines, and a non-negligible impact of the glycerol backbone-tilting, letting the *sn1*-chain penetrate deeper into the opposing leaflet by half a $CH_2$ group. That is, penetration-depth differences due to the ester-linked hydrocarbons at the glycerol backbone, reported previously for gel phase structures also extend to the physiological more relevant fluid phase, but are significantly reduced. Moreover, milk sphingomyelin was found to follow the same linear relationship suggesting a similar tilt of the sphingosine backbone. Complementary performed molecular dynamics simulations revealed that there is always a part of the lipid tails bending back, even if there is a high interdigitation with the opposing chains. This suggests that hydrocarbon chain interdigitation plays only a minor role in transbilayer coupling. For both cases of adaption to chain length mismatch, chain-asymmetry has a large impact on hydrocarbon chain ordering, inducing disorder in the longer of the two hydrocarbons.

**Keywords:** Mixed-chain lipids; Neutron scattering; X-ray scattering; MD simulations

## 1. Introduction

As the main structural constituents of biological membranes, glycerophospholipids and sphingolipids occur in a large variety of species, differing in their hydrophilic heads, hydrophobic tails and backbone structure. A considerable fraction of the most abundant double-chained membrane lipids exhibit distinct compositional differences of their hydrocarbons [1,2]. Particularly, combinations of a saturated and an unsaturated chain are very common for glycerophospholipids and are therefore widely used in membrane mimics. Some of these, and in particular monounsaturated phosphatidylcholines (PCs) like palmitoyl oleoyl PC (POPC) or stearoyl oleoyl PC (SOPC) are therefore well characterized in their fluid phase structures [3]. In contrast, saturated phospholipids with mixed chain lengths are much less abundant and hence less frequently studied. Large chain length asymmetries including long, saturated chains are however frequent in sphingolipids, such as, e.g. sphingomyelin. Sphingomyelin contains a sphingosine backbone of 18 carbons and an acyl chain, which can largely vary in length. Its chain asymmetry and heterogeneity has been shown to impede the formation of liquid-ordered domains in mixtures with cholesterol [4], which might be due to hydrocarbon packing stresses caused either by a penetration of the longer hydrocarbon chain into the opposing leaflet (interdigitation) or by bending the chain back into its host leaflet. Further hydrocarbon chain interdigitation has been also implied in transleaflet coupling of asymmetric lipid bilayers [5–7].

In order to explore the effects of hydrocarbon chain interdigitation versus chain backward bending, we focused on the chemically well-defined stearoyl myristoyl PC (SMPC), myristoyl stearoyl PC (MSPC) and palmitoyl myristol PC (PMPC). These lipids melt close to physiological temperatures, but their melting temperature ($T_m$) depends strongly on the degree of chain length-asymmetry [8]. Interestingly, thermotropic data for SMPC, MSPC and dipalmitoyl PC (DPPC) suggest that the $T_m$ is highest for equal chain lengths, which occurs however not for DPPC, but for a hypothetical lipid with a *sn2*-chain that is about 1.5 carbon units longer than the *sn1*-chain. This is usually attributed to the ester bonds that link the acyl chains to the glycerol backbone, which causes an effective tilting of the glycerol backbone with respect to the bilayer central plane [9,10]; see supplementary Fig. A1 for lipid structure. On the other hand, this suggests that the hydrocarbons of DPPC in the lamellar gel phase are slightly interdigitated. This has been indeed confirmed by experiments recently [11]. Studies of such effects in the physiologically more relevant lamellar fluid phase are currently missing, but needed to address the above mentioned issues of hydrocarbon-mediated transleaflet coupling.

We have therefore studied the fluid lamellar phases of SMPC, MSPC and PMPC using small-angle X-ray and neutron scattering (SAXS/SANS) experiments, exploiting their different contrasts to enhance structural fidelity [12]. In particular, we jointly analyzed scattering data in terms of compositional modeling applying a slightly modified version of the well known scattering density profile (SDP) model [13]. The advanced SDP model in combination with the separated form factor technique [14] allowed us to include also scattering intensities at very low scattering vectors and led us to introduce a hydration layer in the lipid's headgroup region. The new model was validated against DPPC and confirmed previously reported structural parameters. We consecutively focused on the fluid structures of SMPC, MSPC and PMPC and included also monounsaturated POPC, SOPC and milk sphingomyelin (MSM), which is a natural lipid extract with high chain length asymmetry.

For the fluid phase lipids, we found a large decrease of the lipids' backbone tilt compared to the gel phase corresponding to a length difference of about 0.5 carbon units between *sn-2* and *sn-1* chains. Moreover, hydrocarbon chain overlap depends linearly on chain length mismatch for all studied lipids. All-atom molecular dynamics simulations further helped to disentangle interdigitated from backward-bending hydrocarbons. Interestingly, we found that, close to the lipids' backbone, bending back of hydrocarbons into their host leaflet occurs more likely than interdigitation from the opposing leaflet. This suggests that hydrocarbon interdigitation plays only a minor role in interleaflet coupling of chain-asymmetric fluid lipid bilayers.

## 2. Results and Discussion

### 2.1. Introducing a headgroup hydration shell in the scattering model for lipid bilayers

The SDP model simultaneously accounts for small-angle neutron and X-ray data (SANS/SAXS) of lipid bilayers thus enabling a unique combination of the different contrasts offered by the two techniques (see, e.g. [12]). The very backbone of the SDP model is a parsing of the transbilayer structure into quasimolecular fragments, based on molecular dynamics (MD) simulations [13,15]. This leads to a representation of the membrane structure in terms of Gaussian-type volume probability distributions (Fig. A1). The SDP technique has been highly successful in reporting high-resolution membrane structures of numerous glycero- and sphingolipids [3,16–20], including also polyunsaturated phosphatidylcholines [21].

We first implemented the SDP model for a sphere using the separated form factor method [14], which extended the analysis to previously not considered low scattering vectors $q$ (see section 4.3 and appendix A) and performed test on the benchmark-lipid DPPC. It turned out that the model, using published parameters [3], fits very well to our SANS data, but not to the low-$q$ region in SAXS (Fig. 1a,b). In particular, the SAXS intensity minimum at $q \sim 0.02$ Å$^{-1}$ is completely missed by the fit, while a good agreement is obtained for $q > 0.1$ Å$^{-1}$, i.e. the $q$-range reported previously. We also measured an independently prepared sample of DPPC using a SAXSpoint laboratory camera. Although these data are intrinsically more noisy, in particular at low $q$, they clearly agree with synchrotron data and demonstrate that the mismatch of the previous data modeling is a salient feature. Fits to this region have been however attained by other models, which unlike SDP do not depend on the specific composition of the lipid bilayer [22,23]. This indicates that the solution might be an additional degree of freedom in the scattering length density (SLD) profile. Indeed we found that increasing the contrast in the headgroup region , e.g. by decreasing the headgroup volume, drastically improves the agreement to low-$q$ SAXS-data, while having no significant impact on the neutron form factor (data not shown). Note that a similar approach has been reported in [24]. An alternative, and physically realistic way to do this, is to account for the layer of bound water molecules (Fig. 1c,d). In this model we assumed that the water molecules surrounding the polar headgroup take up a more ordered structure than in the bulk, leading to a higher density in this region. Hydration shells of this kind are extensively used for SAXS data analysis of protein solutions [25,26] and have also been predicted for lipid membranes [27]. We implemented hydration water using an error function that adds one layer of more dense water to the water accessible groups of the lipid bilayer as detailed in section 4.3 and appendix A. Our fit estimates the water density in this shell to be 3% higher than in the bulk, which agrees with previous reports on hydration shells for proteins or nucleic acids [25,26].

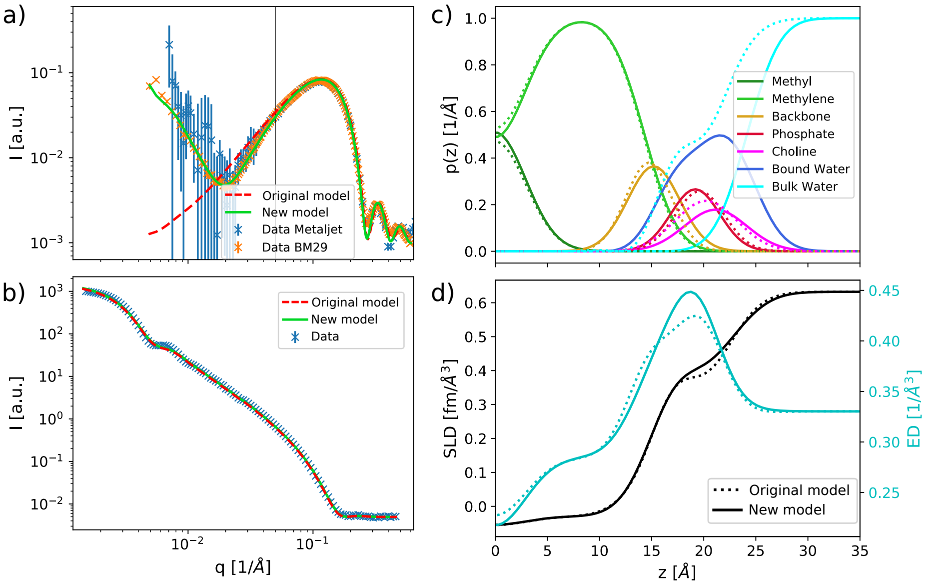

**Figure 1.** Comparison of the present and original SDP-models [3] for DPPC at 50°C. The two models show differences mainly in the low-$q$ region of SAXS (a), whereas they overlap in the case of SANS in 100 % $D_2O$ (b). The vertical black line in (a) marks the lower limit of the accessible range in the original study. (c) shows volume probability distributions $p(z)$ of the lipid moieties through the bilayer profile. The resulting neutron SLD (black) and electron density profiles (cyan) are drawn in (d). Dashed lines correspond to the original, solid lines to the new model.

In achieving this fit we also tested for overfitting or parameter correlations. The SDP-model relies on a rather high number of fitting parameters (i.e. 12 to describe the membrane structure) compared to simpler models using slabs [28] or Gaussian distributions [29]. The high number of adjustable parameters is mostly due to the limited available information about the volumes and structures of the individual moieties in the lipid, which are hardly accessible experimentally and can only be estimated from scattering studies and simulations [30]. Previous studies applying the SDP-model led to no obvious temperature or composition-dependent trends for several parameters, especially for those describing the headgroup ($\sigma_{CG}$, $\sigma_{PCN}$, $D_{H1}$) and the volume fractions ($R_{CG} = V_{CG}/V_H$, $R_{PCN} = V_{PCN}/V_H$, $r = V_{CH3}/V_{CH2}$, $r_{12} = V_{CH}/V_{CH2}$) [3,19] ; see Tabs. A2, A3 for a list of all SDP parameters.

We therefore decided to analyze parameter correlations using a Markov chain Monte Carlo (MCMC) approach as described in section 4.3 (see also [31]). MCMC provides the probability density profiles of the used model parameters and, if plotted in 2 dimensions, correlations between them (Fig. 2). Plateaus of high probability as seen in e.g. (Fig. 2 c), suggest strong correlations, meaning that the quality of the fit will only change minimally if one moves along iso-probability regions. Small differences in the experimental noise can therefore lead to large changes in these parameters, making the estimates of the most likely value (or global minimum) less reliable. In our case, we observed strong correlations between headgroup parameters, such as the positions of carbonyl-glycerol and phosphate groups (Fig. 2a). Also the volume fractions ($R_{CG}$, $R_{PCN}$, $r$) are very flexible parameters insofar that they correlate with the standard deviations of their respective Gaussians ($\sigma_{CG}$, $\sigma_{PCN}$, $\sigma_{CH3}$). Fig. 2b shows for example the correlation between $r$ and $\sigma_{CH3}$. In the following, $\sigma_{CH3}$ will be one of our parameters of interest. Therefore, we decided to fix its volume, along with the ones of the other moieties to the values recently published in [30] (see tables A2, A3), to maximize the comparability between different lipids. This also reduces the number of adjustable parameters for the trans-bilayer structure by 3 (4 in case of mono-unsaturated lipids) compared to previous studies. We also fixed $\sigma_{CholCH_3} = 3$ Å, as has been done before [3], and $\sigma_{CH2} = 2.5$ Å.

Fig. 2c) also shows how the introduction of the hydration shell is in fact an alternative to varying the volume of the headgroup $V_H$. The volume per bound water molecule $V_{BW}$ is linearly correlated with $V_H$, if we keep the headgroup structure constant. Varying either of them is thus a valid approach to increase the headgroup SLD. We choose to include the hydration shell in order to conform to published values for the volumes [30]. Additionally, if we keep the headgroup volume constant ($V_H = 328$ Å$^3$), $V_{BW}$ correlates with the width of the headgroup and thus the number of bound water molecules (shown by the correlation between the distance phosphate to choline $d_{Chol}$ and $V_{BW}$ in Fig. 2d). The distribution shows the highest probability density between $V_{BW} = 29.0 - 29.5$ Å$^3$ for $V_{BW}$, which also leads to a physically realistic range of distances $d_{Chol}$. We chose $V_{BW} = 29.3$ Å$^3$, which is at the peak of the distribution.

Despite the improved fit of SAXS data at $q < 0.1$ Å$^{-1}$ we observed only minor changes in membrane structural parameters (Tab. A2). This can be expected due to the excellent agreement of the previous SDP model for $q > 0.1$ Å$^{-1}$, i.e. for scattering vectors probing distances on the order of the membrane thickness and below. The newly introduced hydration shell gives us an estimate of the number of bound water molecules per lipid. Note that this is not an explicit fitting parameter, but is defined by the integral over the water volume probability density function within the Luzzati thickness, as has been in detail described in [32].The number of bound water molecules we obtained, varied between 9.6 to 12.8 for saturated PCs and MSM, and was about 16 for the more loosely-packed monounsaturated PCs. These numbers agree roughly with previously published values [32,33]. However, there is a wide spread in measured values, mostly due to varying definitions of $n_w$. Also in our case we attribute a large uncertainty to these values, as it is strongly influenced by the choice of other parameters as discussed above.

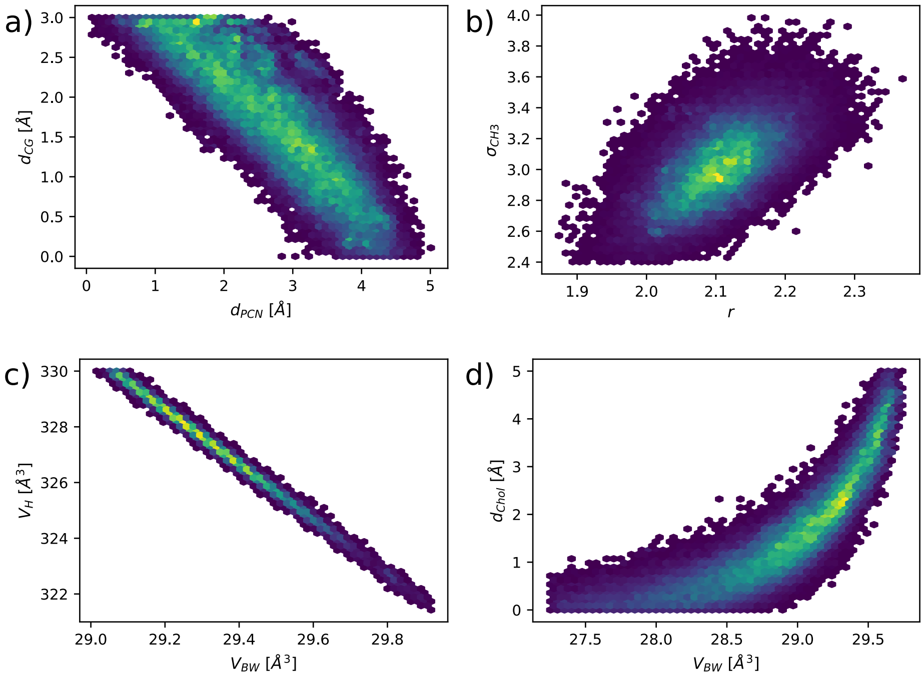

**Figure 2.** Exemplary parameter correlations in the joint SAXS/SANS-analysis of DPPC vesicles, visualised by MCMC sample histograms. Colored spots correspond to Monte Carlo samples, the brighter the color, the more samples are contained in the point, thus corresponding to higher probability. a) shows the correlation between the positions of the carbonyl-glycerol and the phosphate group, b) between terminal methyl relative volume $r$ and distribution width $\sigma_{CH3}$, c) between volume per bound water molecule $V_{BW}$ and headgroup volume $V_H$ (with constant headgroup structure), and d) between $V_{BW}$ and the position of the choline-CH$_3$ group (with constant $V_H$).

### *2.2. Membrane structure and interleaflet hydrocarbon partitioning*

In the next step we applied our modified SDP anaylsis to various chain-asymmetric PCs as well as the highly asymmetric milk-sphingomyelin extract (average acyl chain length: C22:0). Fits and all parameters are reported in the appendix, Figs. A2, A3 and Tabs. A2, A3. High-resolution structural data for POPC and SOPC have been detailed previously [3]. Again we find no substantial modifications to reported structural details upon the application of our model. To the best of our knowledge structural details for MSPC, SMPC, PMPC and MSM have not been reported before, however. Notably, we found that the area per lipid, $A$, of all four lipids is very similar and compares well to that of DPPC. This demonstrates that chain-asymmetry has no major influence on the general packing of these lipids within the bilayer in the biologically most relevant lamellar fluid phase. Substituting the *sn*2-hydrocarbon with an oleoyl chain increases $A$ significantly, in agreement with [3]. The thickness of the bilayer, $D_B$, and the thickness of the hydrocarbon chain region, $2D_C$, in turn vary between MSPC, SMPC, PMPC and MSM according to the total number of methylenes. Interestingly, $D_B = 40.3$ Å for DPPC, MSPC, and SMPC, suggesting that the overall membrane thickness depends for saturated hydrocarbons only on the average number of carbons per chain and is not influenced by even the extreme acyl chain asymmetries of MSPC and SMPC. Note also that the slightly different $2D_C$ values for these three lipids are equal within experimental resolution.

Several fluid phase structures of sphingomyelins have been recently published [20,34], namely palmitoyl-sphingomyelin (PSM), stearoyl-sphingomyelin (SSM) and egg yolk-sphingomyelin (ESM). In both studies the structure of PSM was measured at 45 °C; the reported areas per lipid however differ, possibly due to the different experimental approaches (X-ray surface diffraction on stacks of bilayers vs. SAXS/SANS on vesicles). For ESM, a natural lipid mixture like MSM, but with PSM as its main constituent, the same structure as for PSM was measured [34], suggesting that hydrocarbon chain heterogeneity does not induce a significant disorder in the chain region. For SSM however, the reported $A = 62.5\ \text{Å}^2$ is considerably higher than the one for PSM [20]. Our result for MSM is again higher ($A = 64.8\ \text{Å}^2$), using a similar methodology as reported in [20]. The lateral packing density of sphingomyelin might therefore be directly related to the (average) length of its acyl-chain: PSM/ESM (16:0) < SSM (18:0) < MSM (22:0). Bilayer thickness and terminal methyl overlap are higher for MSM than for the other published lipids, which is expected, again due to its longer acyl chains.

**Table 1.** Results from joint SAXS/SANS data analysis/from MD simulations: Area per lipid $A$, Luzzati thickness $D_B$, hydrophobic thickness $2D_C$, standard deviation of the terminal methyl Gaussian $\sigma_{CH3}$, relative methyl overlap $Y$. The column $\epsilon$ gives an error estimate relative to the values in the table.

| | $\epsilon$ [%] | DPPC | MSPC | SMPC | PMPC | POPC | SOPC | MSM |
|---|---|---|---|---|---|---|---|---|
| $A$ [Å²] | 2 | 63.1 | 62.2 | 62.0 | 62.9 | 67.5 | 68.8 | 64.8 |
| $D_B$ [Å] | 5 | 40.3 | 40.3 | 40.3 | 38.4 | 38.4 | 39.4 | 42.1 |
| $2D_C$ [Å] | 3 | 28.6 | 29.1 | 29.2 | 27.0 | 28.4 | 29.2 | 32.8 |
| $\sigma_{CH3}$ [Å] | 5 | 2.91 | 3.34 | 3.67 | 3.12 | 3.41 | 3.31 | 4.29 |
| $n_W$ | 10 | 9.7 | 11.3 | 12.8 | 12.1 | 16.6 | 15.1 | 9.6 |
| $Y$ | 7 | 0.43 | 0.55 | 0.65 | 0.54 | 0.60 | 0.55 | 0.71 |

In the following we focus on the hydrocarbon chain interdigitation, which can be expected to be significant given the chain asymmetries of the presently studied lipids. Interleaflet interdigitation may, however, also arise from the specific backbone structure of glycerophospholipids, where the ester bonded hydrocarbon at *sn2* protrudes less into the bilayer core even at nominally equal chain length [10]. Here we use the width of the terminal methyl group, $\sigma_{CH3}$, as a measure for hydrocarbon chain interdigitation. $\sigma_{CH3}$ varied significantly for the different lipids studied (Tab. 1). In order to derive a possible correlation between chain asymmetry and $\sigma_{CH3}$, we define the chain length mismatch $\Delta l_C := l_C(sn1) - l_C(sn2)$. Further, we estimated $\Delta l_C$ by assuming $l_C$ to be equal to the half-hydrophobic thickness $D_C$ of the corresponding chain-symmetric lipid bilayers (see Tab. A5). Figure 3 presents the resulting dependence of $\sigma_{CH3}$ on $\Delta l_C$. We observed a nearly linear increase of hydrocarbon overlap with increasing chain length mismatch.

SMPC and MSPC possess *a priori* the same absolute value of chain length mismatch. In this case it is, however, important to take the well-known tilting of the glycerol backbone [9] into account, which effectively lengthens the *sn1* and shortens the *sn2* chain. We therefore introduce a correction $d_{tilt}$ on the chain length-mismatch (Eq. 1).

$$\Delta l_{C,corr} := l_C(sn1) - l_C(sn2) + d_{tilt} \tag{1}$$

We estimate its value by assuming a linear relation between the corrected, absolute chain length mismatch $|\Delta l_{C,corr}|$ and $\sigma_{CH3}$. In order to evaluate the most likely value for $d_{tilt}$, we use an iterative approach, optimizing alternately

$$\sigma_{CH3} = k|\Delta l_{C,corr}| + \sigma_{CH3}^{sym}, \tag{2}$$

and Eq. 1. Here $k$ is the slope and $\sigma_{CH3}^{sym}$ is the terminal methyl width of a hypothetical lipid of equally long chains; for details, see the pseudocode algorithm 1.

The result is shown in the upper panel of Fig. 3, with the value $d_{tilt} = 0.48$ Å. In terms of chain length dependence on the number of carbons (Tab. A5), this corresponds to about half the length of a $CH_2$-segment. The parameters of the linear fit result in $k = 0.20$ and $\sigma_{CH3}^{sym} = 2.75$ Å. The chain overlap thus rises only slowly with the chain length mismatch (20 % of its length), which fits into a bilayer picture of fluid hydrocarbon chains, not directly pointing towards the center, but significantly diverted and/or bent. Note that our analysis indicates that even DPPC has an quite large inherent hydrocarbon interdigitation.

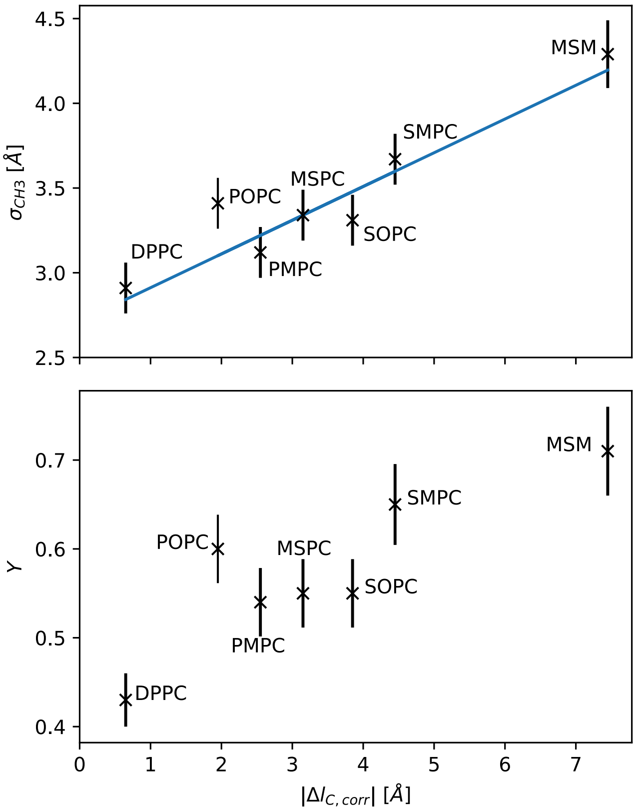

**Figure 3.** Standard deviations $\sigma_{CH3}$ of the Gaussian volume distributions of the terminal methyl groups (upper plot) and relative interdigitation parameters (lower plot), plotted over the corrected chain length mismatch $|\Delta l_{C,corr}|$ of the respective lipids. The upper plot contains a linear regression according to eq. A1. $\sigma_{CH3}$ over uncorrected values $|\Delta l_C|$ are shown in appendix Fig. A4

Preprints (www.preprints.org) | NOT PEER-REVIEWED | Posted: 1 July 2021 doi:10.20944/preprints202107.0039.v1

### 2.3. Quantifying hydrocarbon chain overlap relative to the hydrophobic thickness

The standard deviation of the Gaussian accounting for the terminal methyl groups $\sigma_{CH3}$ gives a measure for hydrocarbon chain interdigitation or, more correct, the terminal methyl dislocation. However, in some cases it might be helpful to describe this quantity relative to the thickness of the hydrocarbon layer to estimate its effect on chain disordering. We therefore introduce the dimensionless parameter $Y$ and connect it to the SDP model, by defining the state $Y = 0$ (no chain overlap) when the volume probability density of the $CH_3$-groups reaches one at the bilayer center. This is the case for $\sigma^0_{CH3} = 2V_{CH3}/(\sqrt{2\pi}A)$. Further we define the state $Y = 1$ by $3\sigma_{CH3} = D_C$, representing a smeared-out state, where the $CH_3$ volume is distributed over the whole hydrocarbon region (fully interdigitated). This leads to the definition

$$Y := \frac{\sigma_{CH3} - \sigma^0_{CH3}}{D_C/3 - \sigma^0_{CH3}}. \tag{3}$$

The extreme states (Y = 0, 1) are most likely purely theoretical. $\sigma^0_{CH3}$ is around 1.4 Å for the studied lipids, while results from section 2.2 suggest that $\sigma_{CH3} \geq 2.75$ Å for PC-lipids. Moreover, also the $\sigma$-values of other molecular groups lie far above this value, suggesting that overall fluctuations of the molecules will not permit a localisation to such an extent. On the other hand, for $Y$ approaching 1 the probability distribution of the $CH_3$ group might no follow a Gaussian shape. In intermediate cases, as for systems used in this study, $Y$ could mark a major characteristic of a bilayer. Here, our results suggest that the relative dislocation of the chain termini also increases monotonously with hydrocarbon chain mismatch (Fig. 3), and can reach up to $\sim$ 70% of hydrocarbon chain thickness. POPC, interestingly does not fit into this picture, having within experimental uncertainty a relative chain overlap similar to that of SOPC or SMPC. This is most likely a signature of the unsaturated hydrocarbon, which increases due to its kink at the *cis* double bond the width of the distribution of the terminal $CH_3$.

### 2.4. Chain interdigitation and back-bending in simulated systems

From our experiments we are not able to distinguish between lipids in the inner in and outer leaflets. Hence, broadening of the $CH_3$-Gaussian could be either caused by interdigitation or by back-bending of the longer hydrocarbon chain. In order to clarify this issue, we performed MD-simulations on DPPC, MSPC, SMPC, PMPC, and dimyristoyl PC (DMPC) to gain access to details in the behavior of the hydrocarbon chains at the bilayer center. Simulation snapshots and the overall volume probability distributions of terminal methyl groups of DPPC, MSPC, SMPC, PMPC are shown in Fig. 4. In all cases the $CH_3$ distributions are centered in the middle of the bilayer, although their widths are broader than our experimental values (Tab. A2). However the trend over the chain length mismatch agrees with our experimental observation. The snapshots show additionally a significant number of chains penetrating deeply into the opposing leaflet for MSPC, PMPC and SMPC.

A closer look into the the shape of the $CH_3$ distribution functions reveals that they actually decay slower than Gaussians (Fig. A5). Separating the distribution into contributions from *sn1* and *sn2*-chains, from inner and outer leaflet (Fig. 5) leads to further insight. In particular, one can see that the deviation from a bell-shaped function is connected to the shape of the distributions of the individual chains, which are slightly asymmetric with a tailing to the back towards their headgroups. In the cases of MSPC, PMPC and MSPC the distributions of the shorter chains from inner and outer leaflet are well separated, while the long chains overlap in the center. In the case of MSPC and PMPC, the long chain distribution functions from opposing leaflets almost perfectly overlap in the center of the lipid bilayer and deviate only in the tailing toward the headgroup region. This suggests that there is a balance between hydrocarbon interdigitation and back-bending in the center of the membrane, while contributions from backward bent chains dominate over interdigitated hydrocarbons when moving closer to the glycerol backbone. This asymmetric part accounts for 8% of the total area of the

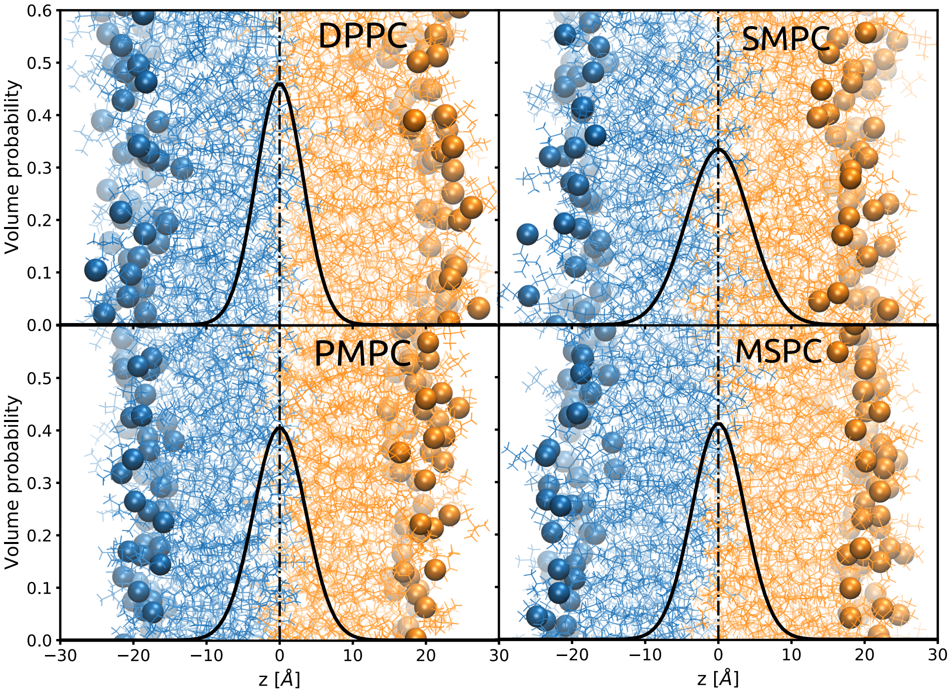

**Figure 4.** Snapshots of MD-simulations for saturated phosphatidylcholines. Spheres mark the positions of phosphorus. The overlaid graphs represent the volume probability distributions of the $CH_3$ groups, summed over all lipids in the bilayer.

distribution (Fig. A5). In the case of SMPC, the long chains penetrate deeper, with the maxima of their distributions in the opposing leaflet. An interesting consequence of the prevalence of contributions from back-bent hydrocarbons further away from the bilayer center comes clear considering that packing defects typically have larger effects on the lateral pressure profile, if they occur closer to the glycerol backbone [35]. That is, even if we do find similar lipid areas for DPPC, SMPC, MSPC, and PMPC, their stored elastic energies may differ significantly and will be dominated by the back-bent hydrocarbons, not by the interdigitating ones.

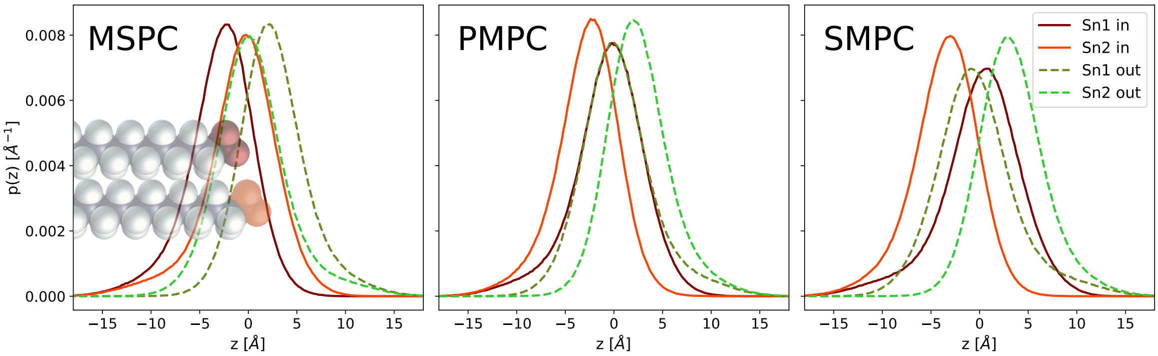

**Figure 5.** Number probability distributions $p(z)$ from MD-simulations of the terminal methyl groups, separately plotted for lipids from inner (left) and outer (right) leaflet, as well as for *sn*1- and *sn*2-chains.

Another effect of the hydrocarbon chain mismatch can be seen in the orientational order parameter $S_{CH}$ of the hydrocarbons, which was also derived from MD simulations. This dimensionless number represents the average orientation of the respective C-H bonds relative to the bilayer normal [36] and approaches 1 for perfectly ordered chains. Hydrocarbons are labelled by the number $n_C$, starting with 1 at the ester bond. In the case of chain-symmetric lipids, the strength of the attractive van der Waals-interactions between the hydrocarbon chains increases with chain length, leading to a

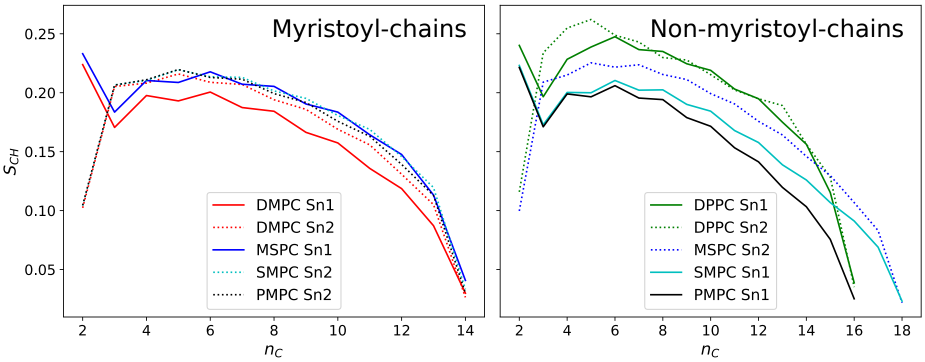

**Figure 6.** Orientational order parameters $S_{CH}$ from MD-simulations for individual lipids and chains.

higher ordered state, as can be seen in the example of DMPC (14 carbons /chain) and DPPC (16 carbons/chain). If there is a chain length-mismatch however, the longer chain lacks its direct neighbor at its tip, decreasing its order. In fact, order parameters of the longer chains in MSPC, SMPC and PMPC are close to the ones of DMPC for low $n_C$ and well below those of DPPC. Again we see a difference between MSPC and SMPC: due to the glycerol-tilt the 18:0 chain in MSPC has a lower effective length difference to its 14:0 chain and is therefore more ordered than in SMPC. On the other hand, the behavior of the short myristoyl-chain is almost identical for all lipids, as they all have a long neighboring chain to optimize van der Waals interactions. Solely the *sn1*-chain in DMPC, being again longer than its *sn2* due to the glycerol-tilt, has slightly lower order parameters.

## 3. Conclusion

We report trans-bilayer structural profiles of free-floating large unilamellar vesicles containing several chain-asymmetric PCs as well as milk sphingomyelin. Additionally, we introduced a shell of hydration water into the well-established SDP model, which allowed us to model low-$q$ SAXS-data conserving previously reported lipid headgroup volumes. For fully saturated PCs we observed no significant effects on overall bilayer structure resulting from the chain asymmetry, except for the overlap of their terminal methyl groups in the membrane center. This overlap displays a linear dependence on the length difference between both acyl chains, if one considers the tilt of the glycerol-backbone. We found that the tilt elongates the *sn*1-chain by 0.48 Å, which is about one third of the value previously reported for gel phases [8]. For PCs with a saturated and an unsaturated chain, we find a poorer agreement with the linear relation between chain length difference and hydrocarbon overlap, which might be a consequence of the kink induced at the double bond. MSM in turn is well described by the model and shows, as expected, the highest hydrocarbon chain overlap of all studied lipids. It has however a lower packing density than fully saturated PCs, which agrees with other recent studies, suggesting that long acyl chains lead to a lower packing density in the case of sphingomyelins.

Using MD simulations, we found that every chain, which does not have an equally long or longer direct neighbor, is significantly more disordered – not only at its tip but over the whole chain length. Moreover, close investigation of the positions of the methyl groups revealed that chains are not distributed symmetrically around a mean position, but have a higher fraction of chains bending back towards their own headgroup. Since, membrane elasticity is more affected by packing defects close to the lipids' backbone this implies that any effect on transleaflet coupling induced by chain asymmetric lipids will be dominated by back-bent hydrocarbons and not by those interdigitating into the opposing leaflet.

## 4. Materials and Methods

### 4.1. Lipids, chemicals and sample preparation

All lipids were purchased in form of powder from Avanti Polar Lipids (Alabaster, AL) and used without further purification. Chloroform and methanol (pro analysis grade) were obtained from Merck KGaA, Darmstadt, Germany. Lipid films were prepared by dissolving weighted amounts in organic solvent chloroform/methanol (2:1, vol/vol) followed by evaporation under a soft $N_2$ stream and overnight storage in a vacuum chamber. The dry filmes were hydrated with ultrapure $H_2O$, $D_2O$ or a mixture of both, and equilibrated for one hour at 50°C followed by 5 freeze-and-thaw cycles using liquid $N_2$ and intermittent vortex-mixing. Large unilamellar vesicles (LUVs) were obtained by 51 extrusions with a hand held mini extruder (Avanti Polar Lipids, Alabaster, AL) using a 100 nm pore diameter polycarbonate filter. Vesicle size and polydispersity was determined via dynamic light scattering using a Zetasizer NANO ZS90 (Malvern Panalytical, Malvern, UK).

### 4.2. Scattering experiments

SANS measurements were performed at D22, Institute Laue-Langevin, Grenoble, France [37]. We measured three configurations at sample-to-detector distances of 1.6, 5.6 and 17.8 m with corresponding collimations of 2.8, 5.6 and 17.8 m and a wavelength of 6 Å $(\Delta\lambda/\lambda = 10\%)$. Data was recorded on $^3$H multidetector of 128 linear sensitive Reuter-Stokes® detector tubes, with a pixel size of 0.8 x 0.8 cm. Samples were filled in Hellma 120-QS cuvettes of 1 mm pathway and measured at 50 °C. Lipid concentrations were 5 mg/ml in 100 % $D_2O$, 10 mg/ml in 75 % $D_2O$ and 15 mg/ml in 50 % $D_2O$. Data were reduced using GRASP (www.ill.eu/users/support-labs-infrastructure/software-scientific-tools/grasp/), performing flat field, solid angle, dead time and transmission correction, normalizing by incident flux and subtracting contributions from empty cell and solvent.

SAXS data were recorded at BM29, ESRF, Grenoble, France (Experiment MX-2282), equipped with a Pilatus3 2M detector, using a photon energy of 15 keV at a sample-to-detector distance of 2.867 m [38]. Samples were measured at a concentration of 10 mg/ml, at 50 °C and exposed for 20 times 2 s in a flow-through quartz capillary of 1 mm light path length. Data reduction and normalisation was done by the automated ExiSAXS system; for subtraction of solvent and capillary contributions SAXSutilities 2 (www.saxsutilities.eu) was used. Additionally DPPC LUVs were measured using a SAXSpoint camera (Anton Paar, Graz, Austria) connected to a MetalJet X-ray generator (Excillum, Kista, Sweden) with a liquid, Ga-rich alloy, jet anode. Data was recorded using an Eiger R 1 M detector system (Dectris, Baden-Daettwil, Switzerland) and reduced via the software SAXSanalyis (Anton Paar).

### 4.3. SDP-modeling of lipid bilayers

Small-angle scattering (SAS) data were analyzed in terms of a probability-density based approach, also known as the scattering density profile (SDP) model, which is frequently used in small-angle scattering and reflectrometry e.g. [13,15,39,40]. We used the same parsing scheme as Kučerka et al.[3] for saturated phosphatidylcholines, describing the volume probability distributions of individual moieties of the lipid molecules by Gaussian distributions (terminal methyls, carbonyl-glycerol backbone, phosphate group, choline-$CH_3$ group) and error-functions (hydrocarbon chains without terminal methyls), see Fig. 1 and appendix A. From these functions, the neutron or X-ray scattering length density profiles can be easily calculated. The model in its current form has been applied to describe SAXS-data from LUVs in the range of scattering vectors, $q$ from 0.1 to 0.6 $Å^{-1}$; lower-$q$ data have been excluded from the SDP analysis. This motivated us to introduce a few adjustments, permitting us to extend the $q$-range by one order of magnitude.

Upon combining the SDP-model, which describes a flat bilayer, with an appropriate model to describe the overall vesicle shape – according to the separated form factor model [14], we found that the calculated intensities do not fit experimental SAXS data in the low-$q$ region (Fig. 1). The position of the first minimum connected to the membrane structure (see Fig. 1a, $q \sim 0.02$ Å$^{-1}$) suggests that the electron density in the head group region is higher than initially thought. One way to account for this, is by introducing a layer of higher density water around the headgroup. This was inspired by previous considerations about lipid bilayers [15] as well as the established necessity to include a hydration layer in protein and nucleic acid models [25]. Hydration water was included into the model using another error-function adjacent to the ones describing the hydrocarbon chains, with the same smearing parameter $\sigma_{CH2}$ and reaching up to the position of the choline-$CH_3$ group in addition of $\sigma_{Chol}$. This ensures that the hydration layer always surrounds the headgroup by roughly one water molecule. We used a width of $d_{shell} = 3.1$ Å around the lipid head group and set the upper limit for the volume per molecule to the bulk water value of 30.28 Å$^3$ (see appendix A4).

The second modification addresses the mismatch of the model with the depth of bilayer-related minima of the X-ray data. We were able to account for this by including a Gaussian polydispersity on the membrane thickness. It is implemented by varying only the width of the hydrocarbon chain region, while keeping all other parameters unchanged. One could attempt to extend the model to a more flexible headgroup for states of different unit cell area, however, as described in the result section. However, one would risk that area-compressed states could end up with an over-filled unit cell. Also, headgroup parameters from scattering data are generally ill-defined and highly correlated; therefore we remained with a static headgroup. A possible physical explanation for this effect is the influence of peristaltic modes, which have been found for this $q$-region in MD-simulations [41]. These fluctuations, however, do not exert the same amplitudes for all wavelengths. This might also explain why our implementation, despite the large improvement in fit quality still did not perfectly match the form factor minima.

We further note that the various volume probability functions in our model do not necessarily overlap perfectly for all configurations of positions and standard deviations, potentially leading to an overfilling of the unit cell which the model would automatically compensate for with "negative water". To have our optimization algorithm automatically avoid these regions, we introduced a penalty on the cost function minimized in the procedure. To do this, we calculate the number of negative water molecules $n_{-H_2O}$ in each iterations and modify the cost function $\chi^2 \rightarrow \chi^2 + n^2_{-H_2O}/\sigma^2_{-H_2O}$. The strength of the penalty can be tuned by adjusting $\sigma^2_{-H_2O}$.

Parameter optimization was done using the Trust Region Reflective algorithm from the SciPy 1.6.2 package [42]. To analyze parameter correlations within the model we used the No-U-Turn Sampler within the PyMC3 package [43,44].

### *4.4. Molecular Dynamics simulations*

At the time of bilayer construction, the three lipids, MSPC, PMPC and SMPC were not available in the CHARMM-GUI web server [45–49]. We therefore first used CHARMM-GUI to construct bilayers of pure distearoyl PC (DSPC) or pure DPPC lipids. Each bilayer had 100 lipids per leaflet (200 lipids total) and was hydrated with 45 water molecules per lipid (without any salt ions). PMPC was then built from the DPPC bilayer by removing the last carbon on the *sn1* chain (C216 in CHARMM36 notation) together with its 3 hydrogens (H16R, H16S, H16T) and the 2 hydrogens bonded to the last-but-one carbon on that same chain (H15R and H15S). Carbon C215 was then changed to hydrogen (H14T) by modifying its atom name, type and charge accordingly to complete the terminal methyl group of the myristoyl chain of the newly created PMPC lipid.

The MSPC and SMPC bilayers were similarly generated from the DSPC bilayer by removing the last 3 carbons and their hydrogens on the *sn1* or *sn2* chains, respectively, then modifying the 15th carbon by removing its hydrogens and changing its name, type and charge to complete the terminal methyl group of the myristoyl chain of the newly created lipids. Additionally, a pure DMPC bilayer was constructed with CHARMM-GUI. The bilayer had 100 lipids per leaflet and was hydrated with 45 water molecules per lipid.

All simulations were run with the NAMD software [50] and the CHARMM36 force field for lipids [51,52]. Each of the bilayer systems, excluding DMPC, was energy minimized for 1200 steps, then simulated for a total of 1 ns with an integration time-step of 1 fs before the production run which employed a time-step of 2 fs. DMPC was equilibrated following CHARMM-GUI's 6-step equilibration protocol. All simulations were run at constant temperature of 50 °C (323K) and pressure of 1 atm maintained by NAMD's Langevin thermostat and Nose-Hoover Langevin piston, respectively. Long-range interactions were modeled with a 10-12 Å Lennard-Jones potential using NAMD's vdwForceSwitching option. All hydrogen bonds were constrained with the rigidbonds parameter set to all and electrostatic interactions were modeled using the Particle Mesh Ewald (PME) method with a grid spacing of 1 Å. The four simulations were run for a total of 1 $\mu$s (MSPC), 0.969 $\mu$s (PMPC) , 1.03 $\mu$s (SMPC) and 0.8 us (DMPC). The first 50 ns were discarded and the rest was used to calculate the number density profile of each system with the density plugin in VMD [53]. The calculation was done at a resolution (slab thickness) of 0.2 Å on trajectory frames spaced 100 ps apart. For comparison, a system of a DPPC bilayer simulated under the same conditions was taken from [54] and its number density profile was calculated following the same procedure.

**Author Contributions:** Conceptualization, Moritz Frewein, Milka Doktorova, Frederick Heberle, Enrico Semeraro and Georg Pabst; Data curation, Milka Doktorova; Formal analysis, Moritz Frewein, Milka Doktorova and Frederick Heberle; Investigation, Moritz Frewein, Milka Doktorova, Haden Scott, Enrico Semeraro and Lionel Porcar; Methodology, Moritz Frewein and Enrico Semeraro; Software, Moritz Frewein; Supervision, Georg Pabst; Visualization, Moritz Frewein; Writing – original draft, Moritz Frewein and Georg Pabst; Writing – review editing, Moritz Frewein, Milka Doktorova, Frederick Heberle, Haden Scott, Enrico Semeraro, Lionel Porcar and Georg Pabst.

**Funding:** This research was supported by the ILL graduate school, PhD no. 181-19. M.D. is supported by the National Institute of General Medical Sciences of the NIH under Award Number F32GM134704. F.A.H. is supported by National Science Foundation grant MCB-1817929 and NIH/National Institute of General Medical Sciences grant R01GM138887

**Acknowledgments:** We thank Petra Pernot for technical assistance at BM29, ESRF.

**Conflicts of Interest:** The authors declare no conflict of interest.

## Abbreviations

The following abbreviations are used in this manuscript:

| | |
|---|---|
| SAXS | Small-angle X-ray scattering |
| SANS | Small-angle neutron scattering |
| SLD | Scattering length density |
| SDP | Scattering density profile |
| MD | Molecular dynamics |
| MCMC | Markov chain Monte Carlo |
| LUV | Large unilamellar vesicle |
| DPPC | 1,2-dipalmitoyl-sn-glycero-3-phosphocholine |
| MSPC | 1-myristoyl-2-stearoyl-sn-glycero-3-phosphocholine |
| SMPC | 1-stearoyl-2-myristoyl-sn-glycero-3-phosphocholine |
| PMPC | 1-palmitoyl-2-myristoyl-sn-glycero-3-phosphocholine |
| MSM | Milk sphingomyelin |

## Appendix A Full SAS-model

The signal in small-angle scattering is described by the absolute square of the form factor, meaning the Fourier-transform of the scattering length density profile (SDP). As the overall vesicle shape and the trans-bilayer structure contribute on different length scales, we can describe them separately and approximate the bilayer as an infinite flat sheet [14]. As we are using error-functions and Gaussians to describe the SDP, the required Fourier transforms are given in the following. Note that the formulas omit the imaginary part of the form factor, which is antisymmetric around the origin and therefore vanishes for a symmetric trans-bilayer profile.

The real part of the Fourier-transform for a slab, described by 2 mirrored error-functions centered around $\mu$, with a width of $d$, a smearing parameter of $\sigma$ and its area normalized to 1, is given by

$$\Re\left\{\frac{1}{2d}\int_{-\infty}^{\infty}\left[\mathrm{erf}\left(\frac{x-\mu+d/2}{\sqrt{2}\sigma}\right)-\mathrm{erf}\left(\frac{x-\mu-d/2}{\sqrt{2}\sigma}\right)\right]\mathrm{e}^{iqx}dx\right\}=\frac{\sin(qd/2)}{qd/2}\mathrm{e}^{-\frac{\sigma^2q^2}{2}}\cos(\mu q) \tag{A1}$$

For the Gaussian distribution centered at $\mu$ and standard deviation $\sigma$ we use the following:

$$\Re\left\{\int_{-\infty}^{\infty}\frac{1}{\sqrt{2\pi}\sigma}\mathrm{e}^{-\frac{(x-\mu)^2}{2\sigma^2}}\mathrm{e}^{iqx}dx\right\}=\mathrm{e}^{-\frac{q^2\sigma^2}{2}}\cos(q\mu) \tag{A2}$$

**Table A1.** Molecular groups described by individual functions
* Sphingosine backbone in the case of MSM

| Abbr. | Content | Function |
|---|---|---|
| CH3 | Terminal methyl group | Gaussian |
| CH2 | Methylene chains | Error-function |
| CG | Carbonyl-Glycerol backbone* | Error-function |
| PCN | Phosphate + CN | Gaussian |
| Chol | Choline-CH3 group | Gaussian |
| BW | Hydration layer | Error-function |

We added up scattering contributions of the parts in table A1, by using the normalized functions (A1) and (A2), weighted by the factors $\frac{V_k}{A}$, $A$ denoting the area per lipid and $V_k$ the volume of the respective moiety. The functions for CH2 and BW are treated differently: They are normalized to fill the whole unit cell area, followed by subtraction of the groups they contain. We applied a polydispersity on the chain-width $D_C$ by summing over a series of form factors with different $D_{C,i}$, weighted by a Gaussian distribution $\mathcal{N}(x|\bar{D_C},\sigma_{poly})$ with a mean $\bar{D_C}$ and standard deviation $\sigma_{poly}$. The average chain-width is calculated by $\bar{D_C}=\frac{n_{CH2}V_{CH2}+2V_{CH3}}{A}$. Contrasts of the individual moieties $k$ are defined by $\Delta\rho_k=\frac{b_k}{V_k}-\rho_{solvent}$, $b$ and $\rho$ denoting scattering length and scattering length density for either radiation (X-rays or neutrons). A graphical representation of all distances between moieties and thicknesses is given in fig. A1.

$$
\begin{aligned}
I(q) \;\propto\; & F_{sphere}(r_{mean}, \sigma_R) \sum_i \mathcal{N}(D_{C,i} | \bar{D_C}, \sigma_{Poly}) \Bigg[ \\
& 2(\Delta\rho_T - \Delta\rho_{CH2}) \frac{V_{CH3} D_{C,i}}{V_{CH2} + V_{CH3}} \mathrm{e}^{-\frac{q^2 \sigma_{CH3}^2}{2}} + \\
& \Delta\rho_{CH2} \frac{1}{q} \mathrm{e}^{-\frac{q^2 \sigma_{CH2}^2}{2}} \sin\left(q D_{C,i}\right) + \\
& 2(\Delta\rho_{CG} - \Delta\rho_{BW}) \frac{V_{CG}}{q A d_{CG}} \mathrm{e}^{-\frac{q^2 \sigma_{CG}^2}{2}} \sin\left(q d_{CG}/2\right) \cos\Big(q(D_{C,i} + d_{CG}/2)\Big) + \\
& 2(\Delta\rho_{PCN} - \Delta\rho_{BW}) \frac{V_{PCN}}{A} \mathrm{e}^{-\frac{q^2 \sigma_{PCN}^2}{2}} \cos\Big(q(D_{C,i} + d_{CG} + d_{PCN}/2)\Big) + \\
& 2(\Delta\rho_{Chol} - \Delta\rho_{BW}) \frac{V_{Chol}}{A} \mathrm{e}^{-\frac{q^2 \sigma_{Chol}^2}{2}} \cos\Big(q(D_{C,i} + d_{CG} + d_{PCN} + d_{Chol}/2)\Big) + \\
& 2\Delta\rho_{BW} \mathrm{e}^{-\frac{q^2 \sigma_{CH2}^2}{2}} \sin\left(q \frac{d_{CG} + d_{PCN} + d_{Chol} + d_{shell}}{2}\right) \cos\left(q(D_{C,i} + \frac{d_{CG} + d_{PCN} + d_{Chol} + d_{shell}}{2})\right) \\
& \Bigg]^2 + I_{inc}
\end{aligned}
$$

To describe the contribution from the overall vesicle shape, we use the Schultz-distributed form factor of a sphere, as described in Kucerka et al. 2007 [55]:

$$
F_{sphere} = \frac{8\pi^2 (z+1)(z+2)}{s^2 q^2} \left\{ 1 - \left(1 + \frac{4q^2}{s^2}\right)^{-(z+3)/2} \cos\left[(z+3) \arctan\left(\frac{2q}{s}\right)\right] \right\}
$$

Mean vesicle radius $R_m$ and polydispersity $\sigma_R$ come in via the auxiliary quantities $s$ and $z$:

$$
s = \frac{R_m}{\sigma_R^2}, \quad z = \frac{R_m^2}{\sigma_R^2} - 1
$$

## Appendix B SDP-model parameters

Tables A2 and A3 contain all information about the SDP-profiles for all studied lipids and references. Parameter notation was chosen to be conform to former publications such as [3].

**Table A2.** Results from joint SAXS-SANS analyis of LUVs containing saturated lipids, comparison to literature values and simulations. $\epsilon$ in the second column denotes relative error-estimates from our SAS-experiments. Quantities not marked with any symbol ($^*$,$^\dagger$ ,$^\ddagger$) were adjustable during the analysis.

| | $\epsilon$ [%] | DPPC$^a$ | DPPC$^b$ | DPPC$^c$ | MSPC$^a$ | MSPC$^c$ | SMPC$^a$ | SMPC$^c$ | PMPC$^a$ | PMPC$^c$ |
|---|---|---|---|---|---|---|---|---|---|---|
| $V_L^*$ [Å³] | | 1232 | 1228.5 | 1209.2 | 1232 | 1210 | 1232 | 1211.1 | 1175.8 | 1155.7 |
| $V_H^*$ [Å³] | | 328 | 331 | 314.4 | 328 | 314.6 | 328 | 315.4 | 328 | 314.7 |
| $r_{CG}^*$ | | 0.44 | 0.40 | 0.48 | 0.44 | 0.48 | 0.44 | 0.49 | 0.44 | 0.48 |
| $r_{PCN}^*$ | | 0.3 | 0.29 | 0.21 | 0.3 | 0.22 | 0.3 | 0.22 | 0.3 | 0.22 |
| $r^*$ | | 2.09 | 1.95 | 2.06 | 2.09 | 2.06 | 2.09 | 2.06 | 2.09 | 2.05 |
| $D_B^\ddagger$ [Å] | 5 | 40.3 | 38.9 | 39.3 | 40.3 | 39.1 | 40.3 | 38.2 | 38.4 | 36.6 |
| $D_{HH}^\ddagger$ [Å] | 3 | 37.5 | 38.4 | 38.4 | 35.7 | 38.4 | 34.8 | 37.6 | 33.9 | 36 |
| $2D_C^\ddagger$ [Å] | 3 | 28.6 | 28.4 | 29.1 | 29.1 | 28.9 | 29.2 | 28.3 | 27.0 | 26.6 |
| $D_{H1}^\ddagger$ [Å] | 20 | 4.5 | 4.97 | 4.7 | 3.3 | 4.8 | 2.8 | 4.7 | 3.5 | 4.7 |
| $A$ [Å²] | 2 | 63.1 | 63.1 | 61.6 | 62.2 | 62 | 62.0 | 63.4 | 62.9 | 63.2 |
| $z_{CG}$ [Å] | 8 | 15.2 | 14.7 | 16.4 | 15.6 | 16.2 | 15.7 | 15.9 | 14.5 | 15 |
| $\sigma_{CG}$ [Å] | 20 | 2.5 | 2.19 | 2.93 | 2.5 | 2.97 | 2.5 | 2.99 | 2.5 | 2.85 |
| $z_{PCN}$ [Å] | 8 | 19.2 | 19.6 | 20.1 | 18.7 | 19.9 | 18.4 | 19.6 | 17.8 | 18.7 |
| $\sigma_{PCN}$ [Å] | 20 | 2.3 | 2.35 | 2.99 | 3.1 | 3.04 | 3.1 | 3.06 | 3.0 | 2.92 |
| $z_{Chol}$ [Å] | 3 | 21.1 | 20.2 | 21.39 | 22.3 | 21.2 | 23.1 | 20.89 | 21.5 | 20.1 |
| $\sigma_{Chol}^\dagger$ [Å] | | 3 | 2.98 | 3.6 | 3 | 3.63 | 3 | 3.63 | 3 | 3.51 |
| $\sigma_{CH2}^\dagger$ [Å] | | 2.5 | 2.47 | 2.83 | 2.5 | 2.88 | 2.5 | 2.88 | 2.5 | 2.73 |
| $\sigma_{CH3}$ [Å] | 5 | 2.9 | 2.94 | 3.23 | 3.3 | 3.59 | 3.7 | 4.32 | 3.1 | 3.58 |
| $\sigma_{poly}$ [%] | 6 | 3.6 | 0 | | 2.9 | | 5.3 | | 3.5 | |
| $V_{W,bound}^\ddagger$ [Å³] | 6 | 29.3 | | | 29.3 | | 29.3 | | 29.3 | |
| $n_W^\ddagger$ | 10 | 9.7 | | | 11.3 | | 12.8 | | 12.1 | |
| $Y^\ddagger$ | 7 | 0.43 | 0.46 | 0.52 | 0.55 | 0.63 | 0.65 | 0.88 | 0.54 | 0.71 |

$^a$ SAS-analyis, this work, $^b$ Kučerka et al. [3], $^c$ MD-simulations, this work, $^*$ fixed according to Nagle et al. [30], $^\dagger$ fixed, $^\ddagger$ calculated quantity.

**Table A3.** Results from joint SAXS-SANS analyis of LUVs containing unsaturated lipids and comparison to literature values. $\epsilon$ in the second column denotes relative error-estimates from our SAS-experiments. Quantities not marked with any symbol ($^*$,$^\dagger$,$^\ddagger$) were adjustable during the analysis.

| | | $\epsilon$ [%] | POPC[a] | POPC[b] | SOPC[a] | SOPC[b] | MSM[a] |
|---|---|---|---|---|---|---|---|
| $V_L^*$ [Å³] | Lipid volume | | 1276.9 | 1275.5 | 1333.1 | 1327.5 | 1336.3 |
| $V_H^*$ [Å³] | Headgroup volume | | 320 | 331 | 328 | 331 | 274 |
| $r_{CG}^*$ | $V_{CG}/V_H$ | | 0.45 | 0.41 | 0.44 | 0.43 | 0.32 |
| $r_{PCN}^*$ | $V_{PCN}/V_H$ | | 0.29 | 0.3 | 0.3 | 0.3 | 0.32 |
| $r^*$ | $V_{CH3}/V_{CH2}$ | | 2.09 | 1.93 | 2.09 | 1.94 | 2.09 |
| $r_{12}^*$ | $V_{CH}/V_{CH2}$ | | 0.8 | 0.8 | 0.8 | 0.8 | 0.8 |
| $D_B^\ddagger$ [Å] | Luzzati bilayer thickness | 5 | 38.4 | 37.9 | 39.4 | 39.0 | 42.1 |
| $D_{HH}^\ddagger$ [Å] | Head-head distance | 3 | 37.5 | 35.9 | 35.7 | 37.0 | 43.0 |
| $2D_C^\ddagger$ [Å] | Hydrophobic thickness | 3 | 28.4 | 28.1 | 29.2 | 29.3 | 32.8 |
| $D_{H1}^\ddagger$ [Å] | $(D_{HH} - 2D_C)/2$ | 20 | 4.6 | 3.91 | 3.3 | 3.9 | 5.1 |
| $A$ [Å²] | Area per lipid | 2 | 67.5 | 67.3 | 68.8 | 68.1 | 64.8 |
| $z_{CG}$ [Å] | $D_C + d_{CG}/2$ | 8 | 15.0 | 14.8 | 15.9 | 15.5 | 18.4 |
| $\sigma_{CG}$ [Å] | | 20 | 2.5 | 2.48 | 2.5 | 2.5 | 2.5 |
| $z_{PCN}$ [Å] | $D_{C,i} + d_{CG} + d_{PCN}/2$ | 8 | 19.1 | 19.3 | 19.0 | 19.5 | 22.1 |
| $\sigma_{PCN}$ [Å] | | 20 | 2.5 | 2.81 | 3.0 | 2.7 | 2.4 |
| $z_{Chol}$ [Å] | $D_C + d_{CG} + d_{PCN} + d_{Chol}/2$ | 3 | 23.4 | 20.3 | 23.0 | 20.5 | 22.1 |
| $\sigma_{Chol}^\dagger$ [Å] | | | 3 | 2.98 | 3 | 2.98 | 3 |
| $\sigma_{CH2}^\dagger$ [Å] | | | 2.5 | 2.50 | 2.5 | 2.5 | 2.5 |
| $\sigma_{CH3}$ [Å] | | 5 | 3.4 | 2.69 | 3.3 | 3.1 | 4.3 |
| $\sigma_{poly}$ [%] | Thickness polydispersity | 6 | 7.9 | 0 | 3.6 | 0 | 3.5 |
| $V_{W,bound}^\ddagger$ [Å³] | Volume per bound water molecule | 6 | 29.9 | | 29.7 | | 29.8 |
| $n_W^\ddagger$ | Number of bound waters | 10 | 16.6 | | 15.1 | | 9.6 |
| $Y^\ddagger$ | Relative methyl overlap | 7 | 0.60 | 0.41 | 0.55 | 0.50 | 0.71 |

[a] SAS-analyis, this work, [b] Kučerka et al. [3], [c] MD-simulations, this work, $^*$ fixed according to Nagle et al. [30], $^\dagger$ fixed, $^\ddagger$ calculated quantity.

The volume of MSM was measured via the vibrating tube principle [56] using a DMA 4500 M density meter (Anton Paar). We measured the density $\rho_s$ of 3 concentrations of MSM at 50°C, prepared as described in section 4.1 in $H_2O$ without extruding (Tab. A4). The volume per MSM molecule was calculated by the following equation [57], using the lipid molecular weight $M_L = 785.034$ g/mol, masses of water $m_w$ and lipid $m_L$ according to the concentrations given in Tab. A4, and a water density $\rho_w$ of 0.98806 g/ml. The density measurements were performed with a nominal accuracy of 0.00005 g/ml.

$$V_L = \frac{M_L}{0.6022\rho_s}\left[1 + \frac{m_w}{m_L}\left(1 - \frac{\rho_s}{\rho_w}\right)\right], \tag{A3}$$

| $c$ [g/l] | $\rho_s$ [g/ml] | $V_L$ [Å$^3$] |
|---|---|---|
| 10 | 0.98798 | 1330 |
| 5 | 0.98803 | 1327 |
| 2.5 | 0.98800 | 1351 |
| 0 | 0.98806 | (pure $H_2O$) |
| | average | 1336 ± 15 |

**Table A4.** Volumetric measurements of MSM vesicles in $H_2O$. $c$... concentration of lipid. $\rho_s$... measured density. $V_L$... volume per MSM molecule according to eq. A3

## Appendix C Evaluation of $\sigma_{CH3}$-data

**Table A5.** Chain lengths $D_C$ at 50 °C in chain-symmetric phosphatidylcholines from previous scattering studies.

| Chain | $D_C$ | Reference |
|---|---|---|
| 14:0 | 12.4 | [3] |
| 16:0 | 14.3 | [3] |
| 18:0 | 16.2 | [3], extrapolated |
| 22:0 | 20.1 | [3], extrapolated |
| 18:1 | 13.0 | [58], extrapolated |
| PSM | 13.3 | [34], 45 °C |

**Algorithm 1** Iterative fitting of the chain length mismatch correction to a linear function
Parameters behind ; in function definitions designate fixed inputs in the optimizations
Data inputs are $\Delta l_C$, $\sigma_{CH3}$

```
function $Flin(k, \sigma^{sym}_{CH3}; |\Delta l_{C,corr}|)$
    return $k|\Delta l_{C,corr}| + \sigma^{sym}_{CH3}$

function $Fcorr(d_{tilt}; \Delta l_C, k, \sigma^{sym}_{CH3})$
    $|\Delta l_{C,corr}| \leftarrow |\Delta l_C + d_{tilt}|$
    return $k|\Delta l_{C,corr}| + \sigma^{sym}_{CH3}$

initialize: $k, \sigma^{sym}_{CH3}, d_{tilt}, |\Delta l_{C,corr}|$
while $|Flin - Fcorr| > \varepsilon$ do
    $k, \sigma^{sym}_{CH3} \leftarrow$ optimize $Flin - \sigma_{CH3} = 0$
    $d_{tilt} \leftarrow$ optimize $Fcorr - \sigma_{CH3} = 0$
end while
```

## Appendix D Supplementary figures

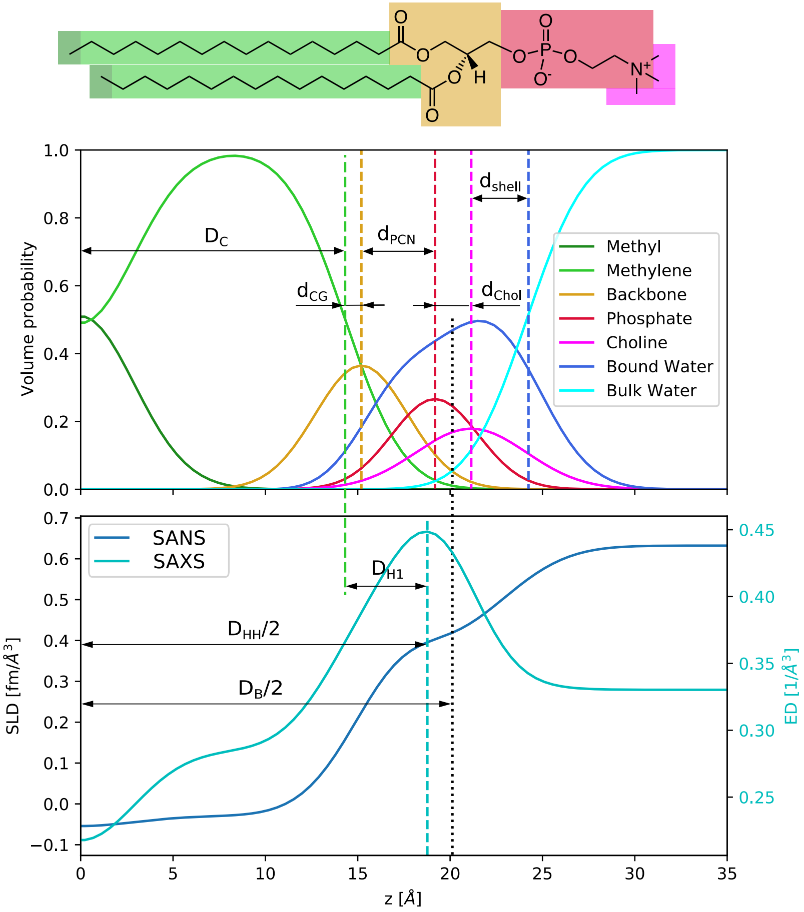

**Figure A1.** Examplary profile of probability distribution functions (top) and scattering length density (SLD)/electron density (ED) profiles (bottom) with definitions of distances used in the SDP-model.

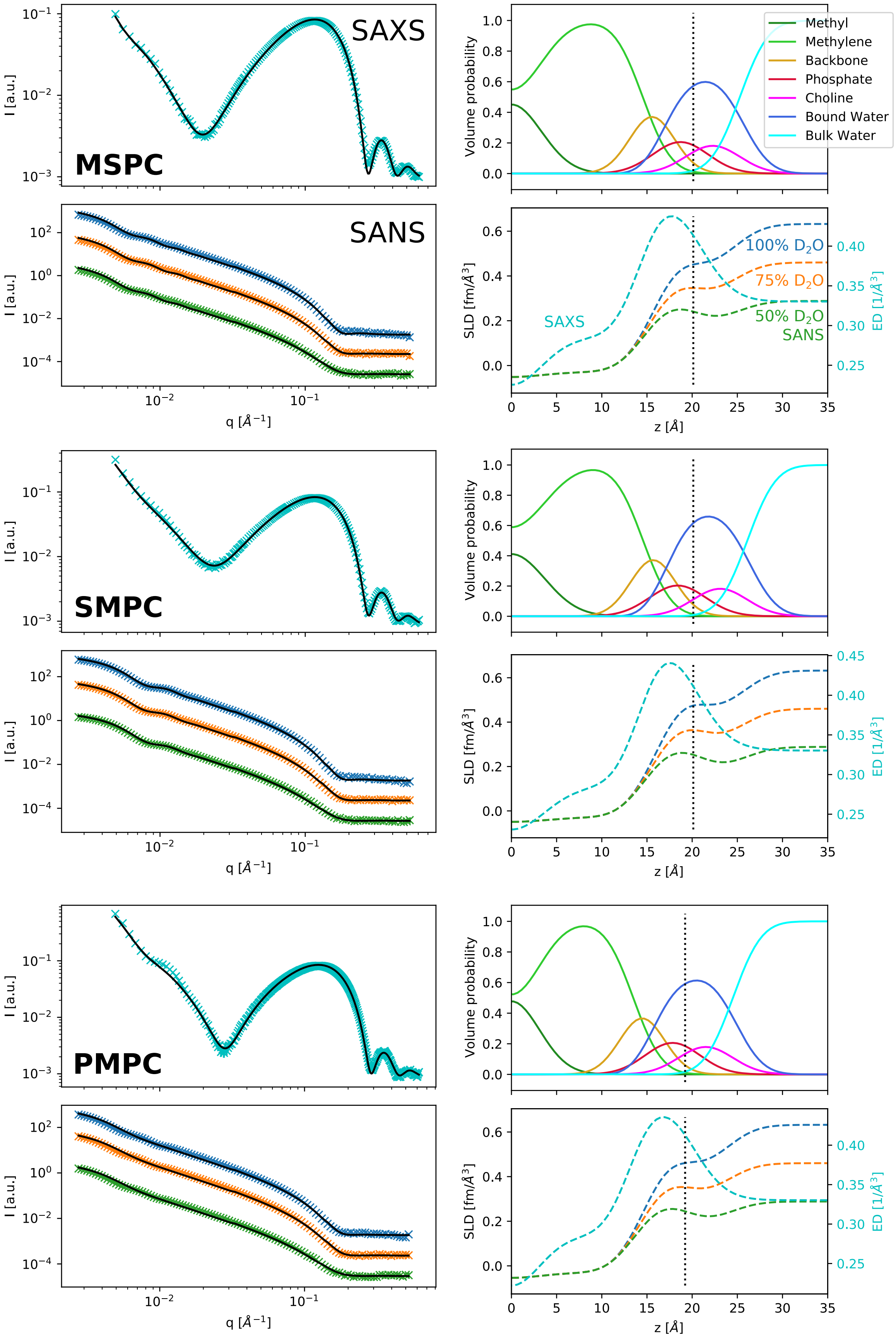

**Figure A2.** SAXS and SANS-data with fits (black lines); SDP-volume probability, electron density and neutron scattering length density profiles for MSPC, SMPC and PMPC. Neutron intensities of different contrasts have been shifted for better visibility.

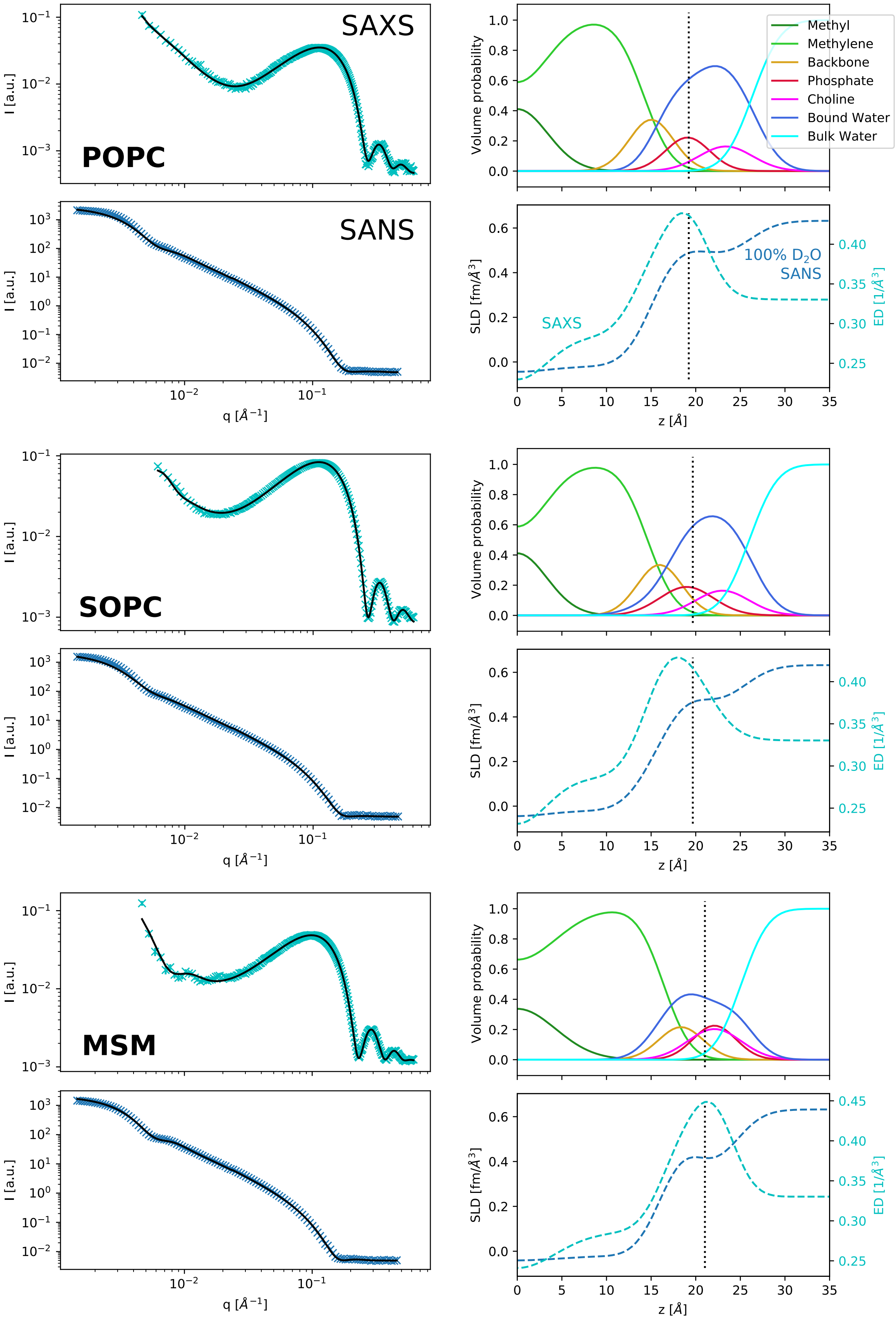

**Figure A3.** SAXS and SANS-data with fits (black lines); SDP-volume probability, electron density and neutron scattering length density profiles for POPC, SOPC and MSM.

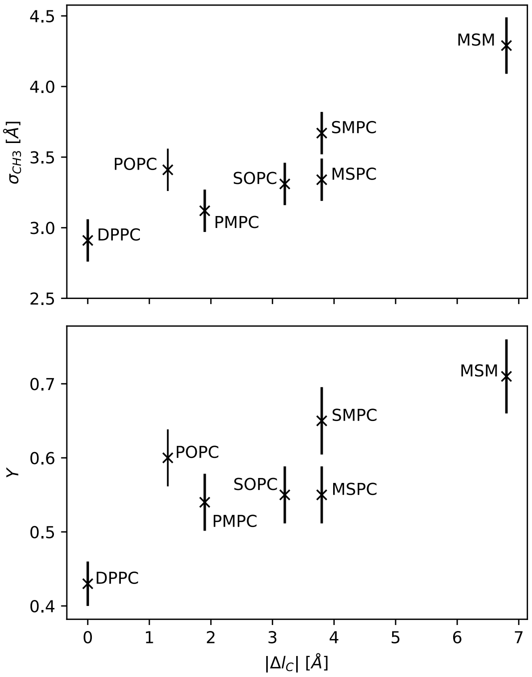

**Figure A4.** Standard deviations $\sigma_{CH3}$ of the Gaussian volume distributions of the terminal methyl groups (upper plot) and relative interdigitation parameters (lower plot), plotted over the chain length mismatch $\Delta l_C$ of the respective lipids.

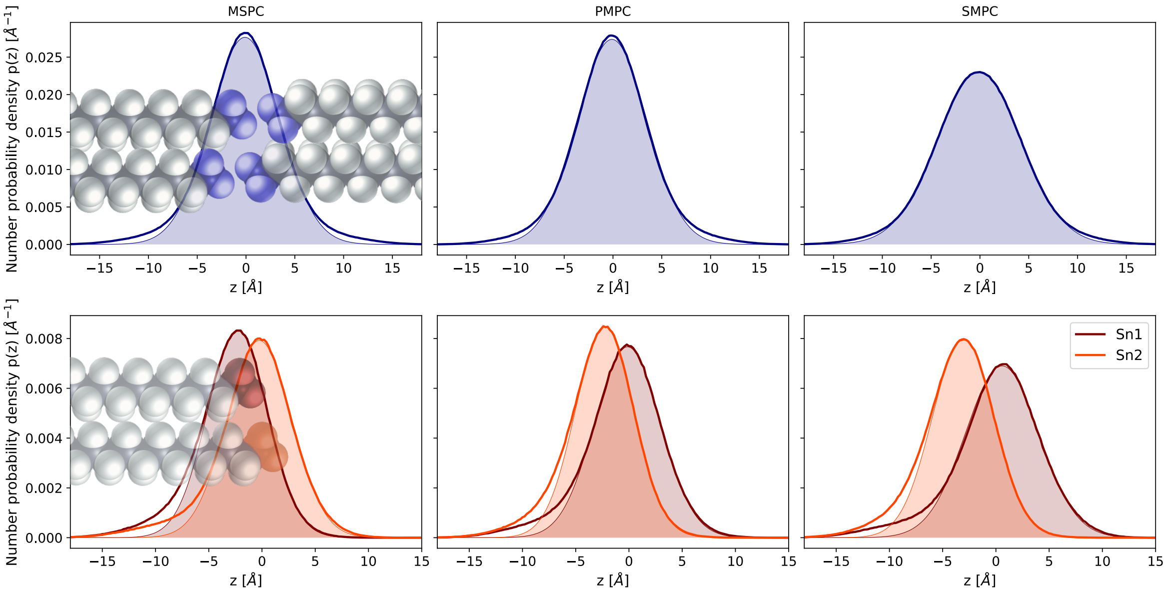

**Figure A5.** The upper panels show the total number probability density distributions of all $CH_3$ groups in the bilayer for the chain-asymmetric saturated lipids MSPC, PMPC and SMPC. Shaded areas and lightly-drawn lines correspond to Gaussian functions fitted to the distribution. In the lower panels the distributions are divided into the $CH_3$ groups of *sn1* and *sn2* chains, showing just the lipids from the left side of the bilayer. Again, Gaussians are inserted in form of shaded areas. They fit almost perfectly in all cases on the right side of the distributions, however to the left there is some mismatch, which causes also the mismatch of the overall distribution. This might be caused by chains bending back towards their headgroups.

## References

1. Lorent, J.H.; Levental, K.R.; Ganesan, L.; Rivera-Longsworth, G.; Sezgin, E.; Doktorova, M.; Lyman, E.; Levental, I. Plasma membranes are asymmetric in lipid unsaturation, packing and protein shape. Nature Chemical Biology **2020**, 16, 644–652. doi:10.1038/s41589-020-0529-6.
2. Ejsing, C.S.; Sampaio, J.L.; Surendranath, V.; Duchoslav, E.; Ekroos, K.; Klemm, R.W.; Simons, K.; Shevchenko, A. Global analysis of the yeast lipidome by quantitative shotgun mass spectrometry. Proceedings of the National Academy of Sciences of the United States of America **2009**, 106, 2136–2141. doi:10.1073/pnas.0811700106.
3. Kučerka, N.; Nieh, M.P.; Katsaras, J. Fluid phase lipid areas and bilayer thicknesses of commonly used phosphatidylcholines as a function of temperature. Biochimica et Biophysica Acta - Biomembranes **2011**, 1808, 2761–2771. doi:10.1016/j.bbamem.2011.07.022.
4. Filippov, A.; Orädd, G.; Lindblom, G. Sphingomyelin structure influences the lateral diffusion and raft formation in lipid bilayers. Biophysical Journal **2006**, 90, 2086–2092. doi:10.1529/biophysj.105.075150.
5. Collins, M.D. Interleaflet coupling mechanisms in bilayers of lipids and cholesterol. Biophysical Journal **2008**, 94, 32–34. doi:10.1529/biophysj.107.124362.
6. May, S. Trans-monolayer coupling of fluid domains in lipid bilayers. Soft Matter **2009**, 5, 3148–3156. doi:10.1039/b901647c.
7. Chiantia, S.; London, E. Acyl Chain length and saturation modulate interleaflet coupling in asymmetric bilayers: Effects on dynamics and structural order. Biophysical Journal **2012**, 103, 2311–2319. doi:10.1016/j.bpj.2012.10.033.
8. Marsh, D. Analysis of the bilayer phase transition temperatures of phosphatidylcholines with mixed chains. Biophysical Journal **1992**, 61, 1036–1040. doi:10.1016/S0006-3495(92)81911-2.
9. Pearson, R.H.; Pascher, I. The molecular structure of lecithin dihydrate. Nature **1979**, 281, 499–501. doi:10.1038/281499a0.
10. Han, X.; Gross, R.W. Plasmenylcholine and Phosphatidylcholine Membrane Bilayers Possess Distinct Conformational Motifs. Biochemistry **1990**, 29, 4992–4996. doi:10.1021/bi00472a032.
11. Nagle, J.F.; Cognet, P.; Dupuy, F.G.; Tristram-Nagle, S. Structure of gel phase DPPC determined by X-ray diffraction. Chemistry and Physics of Lipids **2019**, 218, 168–177. doi:10.1016/j.chemphyslip.2018.12.011.
12. Pabst, G.; Kučerka, N.; Nieh, M.P.; Rheinstädter, M.C.; Katsaras, J. Applications of neutron and X-ray scattering to the study of biologically relevant model membranes. Chemistry and Physics of Lipids **2010**, 163, 460–479. doi:10.1016/j.chemphyslip.2010.03.010.
13. Kučerka, N.; Nagle, J.F.; Sachs, J.N.; Feller, S.E.; Pencer, J.; Jackson, A.; Katsaras, J. Lipid bilayer structure determined by the simultaneous analysis of neutron and X-ray scattering data. Biophysical Journal **2008**, 95, 2356–2367. doi:10.1529/biophysj.108.132662.
14. Pencer, J.; Krueger, S.; Adams, C.P.; Katsaras, J. Method of separated form factors for polydisperse vesicles. Journal of Applied Crystallography **2006**, 39, 293–303. doi:10.1107/S0021889806005255.
15. Wiener, M.C.; White, S.H. Structure of a fluid dioleoylphosphatidylcholine bilayer determined by joint refinement of x-ray and neutron diffraction data. III. Complete structure. Biophysical Journal **1992**, 61, 434–447. doi:10.1016/S0006-3495(92)81849-0.
16. Kučerka, N.; Gallová, J.; Uhríková, D.; Balgavý, P.; Bulacu, M.; Marrink, S.J.; Katsaras, J. Areas of monounsaturated diacylphosphatidylcholines. Biophysical Journal **2009**, 97, 1926–1932. doi:10.1016/j.bpj.2009.06.050.
17. Pan, J.; Heberle, F.A.; Tristram-Nagle, S.; Szymanski, M.; Koepfinger, M.; Katsaras, J.; Kučerka, N. Molecular structures of fluid phase phosphatidylglycerol bilayers as determined by small angle neutron and X-ray scattering. Biochimica et Biophysica Acta - Biomembranes **2012**, 1818, 2135–2148. doi:10.1016/j.bbamem.2012.05.007.
18. Pan, J.; Cheng, X.; Monticelli, L.; Heberle, F.A.; Kučerka, N.; Tieleman, D.P.; Katsaras, J. The molecular structure of a phosphatidylserine bilayer determined by scattering and molecular dynamics simulations. Soft Matter **2014**, 10, 3716–3725. doi:10.1039/c4sm00066h.
19. Kučerka, N.; Van Oosten, B.; Pan, J.; Heberle, F.A.; Harroun, T.A.; Katsaras, J. Molecular structures of fluid phosphatidylethanolamine bilayers obtained from simulation-to-experiment comparisons and

experimental scattering density profiles. Journal of Physical Chemistry B **2015**, 119, 1947–1956. doi:10.1021/jp511159q.

20. Doktorova, M.; Kučerka, N.; Kinnun, J.J.; Pan, J.; Marquardt, D.; Scott, H.L.; Venable, R.M.; Pastor, R.W.; Wassall, S.R.; Katsaras, J.; Heberle, F.A. Molecular Structure of Sphingomyelin in Fluid Phase Bilayers Determined by the Joint Analysis of Small-Angle Neutron and X-ray Scattering Data. Journal of Physical Chemistry B **2020**, 124, 5186–5200. doi:10.1021/acs.jpcb.0c03389.
21. Marquardt, D.; Heberle, F.A.; Pan, J.; Cheng, X.; Pabst, G.; Harroun, T.A.; Kučerka, N.; Katsaras, J. The structures of polyunsaturated lipid bilayers by joint refinement of neutron and X-ray scattering data. Chemistry and Physics of Lipids **2020**, 229. doi:10.1016/j.chemphyslip.2020.104892.
22. Brzustowicz, M.R.; Brunger, A.T. X-ray scattering from unilamellar lipid vesicles. Journal of Applied Crystallography **2005**, 38, 126–131. doi:10.1107/S0021889804029206.
23. Konarev, P.V.; Gruzinov, A.Y.; Mertens, H.D.T.; Svergun, D.I. Restoring structural parameters of lipid mixtures from small-angle X-ray scattering data. Journal of Applied Crystallography **2021**, 54, 169–179. doi:10.1107/s1600576720015368.
24. Heberle, F.A.; Doktorova, M.; Scott, H.L.; Skinkle, A.D.; Waxham, M.N.; Levental, I. Direct label-free imaging of nanodomains in biomimetic and biological membranes by cryogenic electron microscopy. Proceedings of the National Academy of Sciences **2020**, 117, 19943–19952. doi:10.1073/pnas.2002200117.
25. Zaccai, G. Hydration shells with a pinch of salt. Biopolymers **2013**, 99, 233–238. doi:10.1002/bip.22154.
26. Spinozzi, F.; Ferrero, C.; Ortore, M.G.; De Maria Antolinos, A.; Mariani, P. GENFIT: Software for the analysis of small-angle X-ray and neutron scattering data of macro-molecules in solution. Journal of Applied Crystallography **2014**, 47, 1132–1139. doi:10.1107/S1600576714005147.
27. Wiener, M.C.; White, S.H. Fluid bilayer structure determination by the combined use of x-ray and neutron diffraction. II. "Composition-space" refinement method. Biophysical Journal **1991**, 59, 174–185. doi:10.1016/S0006-3495(91)82209-3.
28. Tan, L.; Elkins, J.G.; Davison, B.H.; Kelley, E.G.; Nickels, J. Implementation of a self-consistent slab model of bilayer structure in the SasView suite . Journal of Applied Crystallography **2021**, 54, 363–370. doi:10.1107/s1600576720015526.
29. Pabst, G.; Katsaras, J.; Raghunathan, V.A.; Rappolt, M. Structure and interactions in the anomalous swelling regime of phospholipid bilayers. Langmuir **2003**, 19, 1716–1722. doi:10.1021/la026052e.
30. Nagle, J.F.; Venable, R.M.; Maroclo-Kemmerling, E.; Tristram-Nagle, S.; Harper, P.E.; Pastor, R.W. Revisiting Volumes of Lipid Components in Bilayers. Journal of Physical Chemistry B **2019**, 123, 2697–2709. doi:10.1021/acs.jpcb.8b12010.
31. Frewein, M.P.K.; Rumetshofer, M.; Pabst, G. Global small-angle scattering data analysis of inverted hexagonal phases. Journal of Applied Crystallography **2019**, 52, 403–414. doi:10.1107/S1600576719002760.
32. Tristram-Nagle, S., Use of X-Ray and Neutron Scattering Methods with Volume Measurements to Determine Lipid Bilayer Structure and Number of Water Molecules/Lipid. In Membrane Hydration: The Role of Water in the Structure and Function of Biological Membranes; Disalvo, E.A., Ed.; Springer International Publishing: Cham, 2015; pp. 17–43. doi:10.1007/978-3-319-19060-0_2.
33. Nickels, J.D.; Katsaras, J., Water and Lipid Bilayers. In Membrane Hydration: The Role of Water in the Structure and Function of Biological Membranes; Disalvo, E.A., Ed.; Springer International Publishing: Cham, 2015; pp. 45–67. doi:10.1007/978-3-319-19060-0_3.
34. Arsov, Z.; González-Ramírez, E.J.; Goñi, F.M.; Tristram-Nagle, S.; Nagle, J.F. Phase behavior of palmitoyl and egg sphingomyelin. Chemistry and Physics of Lipids **2018**, 213, 102–110. doi:10.1016/j.chemphyslip.2018.03.003.
35. Cantor, R.S. Lipid composition and the lateral pressure profile in bilayers. Biophysical Journal **1999**, 76, 2625–2639. doi:10.1016/S0006-3495(99)77415-1.
36. Capponi, S.; Freites, J.A.; Tobias, D.J.; White, S.H. Interleaflet mixing and coupling in liquid-disordered phospholipid bilayers. Biochimica et Biophysica Acta - Biomembranes **2016**, 1858, 354–362. doi:10.1016/j.bbamem.2015.11.024.
37. Pabst, G.; Frewein, M.P.K.; Gerelli, Y.; Marx, L.; Porcar, L.; Scott, H.; Semeraro, E.F. Hydrocarbon Chain-Mediated Transleaflet Coupling in Asymmetric Lipid Vesicles. Institute Laue-Langevin doi:10.5291/ILL-DATA.9-13-822, 2019.

38. Pernot, P.; Brennich, M.; Tully, M. The rise of BioSAXS at the ESRF: BM29 beamline for SAXS on proteins in solution. Acta Crystallographica Section A **2018**, 74, a7. doi:10.1107/S0108767318099920.
39. Nagle, J.F.; Tristram-Nagle, S. Lipid bilayer structure. Current opinion in structural biology **2000**, 10, 474–80. doi:10.1016/s0959-440x(00)00117-2.
40. Shekhar, P.; Nanda, H.; Lösche, M.; Heinrich, F. Continuous distribution model for the investigation of complex molecular architectures near interfaces with scattering techniques. Journal of Applied Physics **2011**, 110, 1–10. doi:10.1063/1.3661986.
41. Lindahl, E.; Edholm, O. Mesoscopic undulations and thickness fluctuations in lipid bilayers from molecular dynamics simulations. Biophysical Journal **2000**, 79, 426–433. doi:10.1016/S0006-3495(00)76304-1.
42. Virtanen, P.; Gommers, R.; Oliphant, T.E.; Haberland, M.; Reddy, T.; Cournapeau, D.; Burovski, E.; Peterson, P.; Weckesser, W.; Bright, J.; van der Walt, S.J.; Brett, M.; Wilson, J.; Millman, K.J.; Mayorov, N.; Nelson, A.R.; Jones, E.; Kern, R.; Larson, E.; Carey, C.J.; Polat, ; Feng, Y.; Moore, E.W.; VanderPlas, J.; Laxalde, D.; Perktold, J.; Cimrman, R.; Henriksen, I.; Quintero, E.A.; Harris, C.R.; Archibald, A.M.; Ribeiro, A.H.; Pedregosa, F.; van Mulbregt, P.; Vijaykumar, A.; Bardelli, A.P.; Rothberg, A.; Hilboll, A.; Kloeckner, A.; Scopatz, A.; Lee, A.; Rokem, A.; Woods, C.N.; Fulton, C.; Masson, C.; Häggström, C.; Fitzgerald, C.; Nicholson, D.A.; Hagen, D.R.; Pasechnik, D.V.; Olivetti, E.; Martin, E.; Wieser, E.; Silva, F.; Lenders, F.; Wilhelm, F.; Young, G.; Price, G.A.; Ingold, G.L.; Allen, G.E.; Lee, G.R.; Audren, H.; Probst, I.; Dietrich, J.P.; Silterra, J.; Webber, J.T.; Slavič, J.; Nothman, J.; Buchner, J.; Kulick, J.; Schönberger, J.L.; de Miranda Cardoso, J.V.; Reimer, J.; Harrington, J.; Rodríguez, J.L.C.; Nunez-Iglesias, J.; Kuczynski, J.; Tritz, K.; Thoma, M.; Newville, M.; Kümmerer, M.; Bolingbroke, M.; Tartre, M.; Pak, M.; Smith, N.J.; Nowaczyk, N.; Shebanov, N.; Pavlyk, O.; Brodtkorb, P.A.; Lee, P.; McGibbon, R.T.; Feldbauer, R.; Lewis, S.; Tygier, S.; Sievert, S.; Vigna, S.; Peterson, S.; More, S.; Pudlik, T.; Oshima, T.; Pingel, T.J.; Robitaille, T.P.; Spura, T.; Jones, T.R.; Cera, T.; Leslie, T.; Zito, T.; Krauss, T.; Upadhyay, U.; Halchenko, Y.O.; Vázquez-Baeza, Y. SciPy 1.0: fundamental algorithms for scientific computing in Python. Nature Methods **2020**, 17, 261–272, [1907.10121]. doi:10.1038/s41592-019-0686-2.
43. Hoffman, M.D.; Gelman, A. The no-U-turn sampler: Adaptively setting path lengths in Hamiltonian Monte Carlo. Journal of Machine Learning Research **2014**, 15, 1593–1623, [1111.4246].
44. Salvatier, J.; Wiecki, T.V.; Fonnesbeck, C. Probabilistic programming in Python using PyMC3. PeerJ Computer Science **2016**, 2016, 1–24, [1507.08050]. doi:10.7717/peerj-cs.55.
45. Jo, S.; Kim, T.; Iyer, V.G.; Im, W. CHARMM-GUI: A web-based graphical user interface for CHARMM. Journal of Computational Chemistry **2008**, 29. doi:10.1002/jcc.20945.
46. Lee, J.; Cheng, X.; Swails, J.M.; Yeom, M.S.; Eastman, P.K.; Lemkul, J.A.; Wei, S.; Buckner, J.; Jeong, J.C.; Qi, Y.; Jo, S.; Pande, V.S.; Case, D.A.; Brooks, C.L.; MacKerell, A.D.; Klauda, J.B.; Im, W. CHARMM-GUI Input Generator for NAMD, GROMACS, AMBER, OpenMM, and CHARMM/OpenMM Simulations Using the CHARMM36 Additive Force Field. Journal of Chemical Theory and Computation **2016**, 12. doi:10.1021/acs.jctc.5b00935.
47. Brooks, B.R.; Brooks, C.L.; Mackerell, A.D.; Nilsson, L.; Petrella, R.J.; Roux, B.; Won, Y.; Archontis, G.; Bartels, C.; Boresch, S.; Caflisch, A.; Caves, L.; Cui, Q.; Dinner, A.R.; Feig, M.; Fischer, S.; Gao, J.; Hodoscek, M.; Im, W.; Kuczera, K.; Lazaridis, T.; Ma, J.; Ovchinnikov, V.; Paci, E.; Pastor, R.W.; Post, C.B.; Pu, J.Z.; Schaefer, M.; Tidor, B.; Venable, R.M.; Woodcock, H.L.; Wu, X.; Yang, W.; York, D.M.; Karplus, M. CHARMM: The biomolecular simulation program. Journal of Computational Chemistry **2009**, 30. doi:10.1002/jcc.21287.
48. Wu, E.L.; Cheng, X.; Jo, S.; Rui, H.; Song, K.C.; Dávila-Contreras, E.M.; Qi, Y.; Lee, J.; Monje-Galvan, V.; Venable, R.M.; Klauda, J.B.; Im, W. CHARMM-GUI Membrane Builder toward realistic biological membrane simulations. Journal of Computational Chemistry **2014**, 35. doi:10.1002/jcc.23702.
49. Lee, J.; Patel, D.S.; Ståhle, J.; Park, S.J.; Kern, N.R.; Kim, S.; Lee, J.; Cheng, X.; Valvano, M.A.; Holst, O.; Knirel, Y.A.; Qi, Y.; Jo, S.; Klauda, J.B.; Widmalm, G.; Im, W. CHARMM-GUI Membrane Builder for Complex Biological Membrane Simulations with Glycolipids and Lipoglycans. Journal of Chemical Theory and Computation **2019**, 15. doi:10.1021/acs.jctc.8b01066.
50. Phillips, J.C.; Hardy, D.J.; Maia, J.D.C.; Stone, J.E.; Ribeiro, J.V.; Bernardi, R.C.; Buch, R.; Fiorin, G.; Hénin, J.; Jiang, W.; McGreevy, R.; Melo, M.C.R.; Radak, B.K.; Skeel, R.D.; Singharoy, A.; Wang, Y.; Roux, B.; Aksimentiev, A.; Luthey-Schulten, Z.; Kalé, L.V.; Schulten, K.; Chipot, C.; Tajkhorshid, E. Scalable molecular dynamics on CPU and GPU architectures with NAMD. The Journal of Chemical Physics **2020**, 153. doi:10.1063/5.0014475.

51. Klauda, J.B.; Venable, R.M.; Freites, J.A.; O'Connor, J.W.; Tobias, D.J.; Mondragon-Ramirez, C.; Vorobyov, I.; MacKerell, A.D.; Pastor, R.W. Update of the CHARMM All-Atom Additive Force Field for Lipids: Validation on Six Lipid Types. The Journal of Physical Chemistry B **2010**, 114. doi:10.1021/jp101759q.
52. Klauda, J.B.; Monje, V.; Kim, T.; Im, W. Improving the CHARMM Force Field for Polyunsaturated Fatty Acid Chains. The Journal of Physical Chemistry B **2012**, 116. doi:10.1021/jp304056p.
53. Humphrey, W.; Dalke, A.; Schulten, K. VMD: Visual molecular dynamics. Journal of Molecular Graphics **1996**, 14. doi:10.1016/0263-7855(96)00018-5.
54. Doktorova, M.; Harries, D.; Khelashvili, G. Determination of bending rigidity and tilt modulus of lipid membranes from real-space fluctuation analysis of molecular dynamics simulations. Physical Chemistry Chemical Physics **2017**, 19. doi:10.1039/C7CP01921A.
55. Kučerka, N.; Pencer, J.; Sachs, J.N.; Nagle, J.F.; Katsaras, J. Curvature effect on the structure of phospholipid bilayers. Langmuir **2007**, 23, 1292–1299. doi:10.1021/la062455t.
56. Kratky, O.; Leopold, H.; Stabinger, H. [5] The determination of the partial specific volume of proteins by the mechanical oscillator technique. Methods in Enzymology **1973**, 27, 98–110. doi:10.1016/S0076-6879(73)27007-6.
57. Hallinen, K.M.; Tristram-Nagle, S.; Nagle, J.F. Volumetric stability of lipid bilayers. Physical Chemistry Chemical Physics **2012**, 14, 15452–15457. doi:10.1039/c2cp42595e.
58. Pan, J.; Tristram-Nagle, S.; Kučerka, N.; Nagle, J.F. Temperature dependence of structure, bending rigidity, and bilayer interactions of dioleoylphosphatidylcholine bilayers. Biophysical Journal **2008**, 94, 117–124. doi:10.1529/biophysj.107.115691.